GNSS Interference Monitoring from LEO using the Spire Constellation

Patrick Ellis [(1)], Vladimir Irisov [(1)], Giacomo Pojani [(1)], Stefano Binda [(2)], Hina Khan [(1)], Jeroen Cappaert [(1)], Takayuki Yuasa [(1)], Oleguer Nogués Correig [(1)]

[(1)] Spire Global, Skypark 6, 64-72 Finnieston Square G3 8ET Glasgow UK, +44 (0)141 343 9133, patrick.ellis@spire.com
[(2)]ESA ESTEC, Keplerlaan 1, PO Box 299 NL-2200 AG Noordwijk, The Netherlands, +31 71 565 4105, stefano.binda@esa.int

ABSTRACT

In recent years effective jamming of GNSS user receivers, purposely and not, have increased across the world. These jammers, generically referred to as GNSS Radio-Frequency Interference (RFI) sources, degrade the quality, reliability, and usability of GNSS Position, Navigation, and Timing (PNT) services. Knowledge of the power, location, and directionality of these jamming events can significantly help local entities maintain safe and consistent activities.

Over the past 10 years, Spire has deployed a large LEO constellation of nanosatellites that have harvested RF data in areas such as soil moisture, ocean winds, and refractivity profiles. This paper represents Spire's first efforts to add GNSS jamming detection and geolocation by repurposing ~40 GNSS Intermediate Frequency (IF) collection capable receiver payloads originally designed for GNSS Reflectometry (GNSS-R) and GNSS Radio Occultation (GNSS-RO) satellites.

A fundamental prerequisite of geolocation is precise PNT knowledge across multiple IF-collecting platforms. Through a public and controlled collection done at the L1 frequency in the United States, the quality of the PNT and receiver of Spire's GNSS-R/GNSS-RO satellites was verified, and geolocation was proven capable. This work was completed in partnership with ESA through the NAVISP Element 2 framework, co-funded by the UK Space Agency.

1 INTRODUCTION

Geolocation requires precise PNT knowledge across multiple IF-collecting platforms, circumstantial transceiver geometry, and a solution choice from a suite of algorithmic solutions that vary in effectiveness pending on the collection scenario. From a technical requirements standpoint, the ephemeris accuracy, timing accuracy, and integrity of the raw IF collected needs to be sufficient to provide meaningful geolocation results.

The typical post-processing geolocation mission is depicted in Figure 1. The end user stipulates an area of interest, frequency of interest, time frame of collection, and the signals of interest. Payloads are then tasked, and downlinks scheduled. IF data is then downlinked where post processing and report generation is finished. All stages of this processed are controlled by Spire except for the transmission of the signal. This paper showcases results stemming from a collection done over several days in the state of Nevada in the USA at the L1/L2 frequency utilizing 24 of Spire's GNSS-R/GNSS-RO satellites capturing over 12 minutes of captured IF data at both the L1 and L2 frequency.

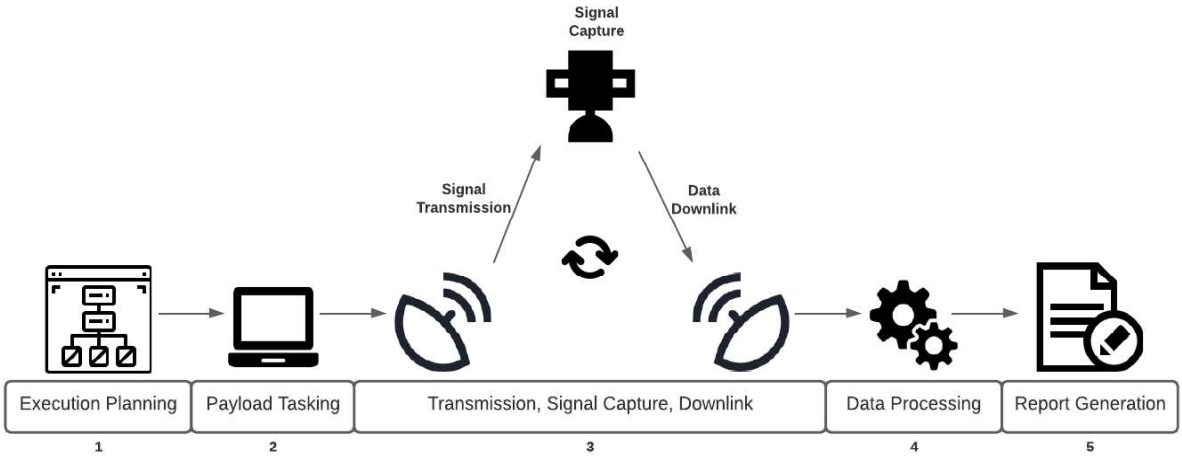

Figure 1- Typical collection methodology.

The transmitted signal was a Continuous Wave (CW) whose two locations were given beforehand in a public flight advisory notice by the Federal Aviation Administration (FAA). This allowed precise determination of receiver frequency offset, the on-board navigation solution, and geolocation. From a technical standpoint, the PNT solution and the raw IF collected needs to be of sufficient accuracy to provide geolocation results with meaningful confidence.

The ephemeral accuracy is posed as a comparison between the On-Board clock-orbit Solution (OBS) and the Precise Orbit Determination (POD) calculated on the ground after collections is made. While POD has its own errors, it generally is in the level of decimeter accuracy. Therefore, it may be regarded as ground truth as its errors are one or two orders of magnitude smaller than those of the OBS. Geolocation is done using a proprietary Single Satellite Geolocation (SSG) algorithm that efficiently maps Doppler estimates to a geolocation fix in nonlinear filtering methodology. The provided dataset is a canonical test of geolocation capability at the L1/L2 band utilizing Spire's GNSS-R and GNSS-RO satellites. Theoretical performance bounds in the form of the Cramer-Rao Lower Bound (CRLB) of geolocation precision are provided in anticipation of multiple satellites simultaneously collecting the same signals. Geolocation algorithms leverage Time and Frequency Differences Of Arrival (TFDOA) measurements of received RFI. The impact on the CRLB of the accuracy of these measurements and of the on-board position and time estimates is presented.

2 SPIRE ASSETS

Spire has ~40 3U GNSS-RO satellites and four GNSS-R satellites available for localized spectrum monitoring. IF signals from each RF front-end channel are stored on the DDR SDRAM of Spire-designed GNSS receiver, STRATOS. In nominal GNSS-RO/GNSS-R observation mode, STRATOS then processes the IF data for real-time navigation and observations of occultation events, grazing-angle reflection events, etc. In offline processing, one can use IF data for a variety of applications, including spectrum monitoring.

2.1 Receivers

Spire's current main Earth observation instrument to be used in the GNSS RFI monitoring demonstration is the Spire-designed STRATOS v1 science-grade GNSS receiver. STRATOS v1 is an advanced, low-power, software-defined, multi-frequency GNSS receiver. It is an open-loop receiver with FPGA-based acceleration of signal processing. This receiver can tune its RF front-end to all L-band GNSS constellations, including GPS, GLONASS, Galileo, QZSS, and BeiDou. The receiver computes the satellite Position Velocity Time (PBT) solution at 1 Hz data rate or higher. The STRATOS v1 has the capability to store the IF data for up to several minutes for post-processing on ground. More recently, new STRATOS v2 GNSS receivers have been designed and launched which

offer the additional ability to sample all frequencies from ~1100 to 1600 MHz with an instantaneous bandwidth of 10 MHz.

2.2 Antennas

Spire's GNSS satellites have one of several possible antenna configurations for GNSS-R and GNSS-RO. Their antennas are generally facing the horizon with a wide azimuthal beampattern and a narrow elevation. Spire GNSS-R satellites carry one wide-field-of-view zenith-facing antenna (called "POD" antenna), and two nadir-facing narrow-field-of-view high-gain antennas (called "R" antennas). Figure 2 shows an example of a GNSS-R satellite.

Figure 2 - GNSS-R satellite. (Left) Physical location of the POD antenna is on the very top of the satellite while the GNSS-R antennas are on the downward facing panels at the bottom. (Right) GNSS-R satellite in testing chamber placed here for visualization purposes.

Spire GNSS-RO satellites carry one wide-field-of-view zenith-facing antenna (called precise orbit determination antenna or POD), and one or two Earth-limb-facing narrow-field-of-view high-gain antennas (called "RO" antennas). These antennas are generally oriented North/South. Figure 3 shows an example of GNSS-RO satellite.

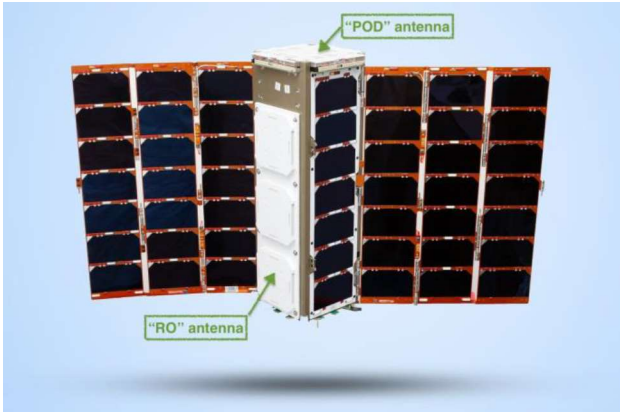

Figure 3 - GNSS-RO satellite. The second RO antennas are attached to the opposite sides of the spacecraft body (the second antenna is not visible in this picture).

3 DATASET

Spire was able to schedule and coordinate a collection of two emitters transmitting CWs at the L1 and L2 frequencies, whose locations are known. This posed as a perfect test scenario to evaluate Spire's GNSS receiver frequency offset, the OBS in terms of Position Velocity Time (PVT) accuracy, and post-processing geolocation capabilities. The collection was done in the Nevada Test and Training Range, NV USA. A NOTAM public flight advisory of GNSS interference was issued for this test and

is publicly available. The relevant information is extracted and listed below.

Location: *Centered at 374117N1161549W or the BTY VOR 007 degree radial at 58 NM*
Dates: *25-27 Jan 22 DLY 2230Z-2359Z*
01-04 Feb 22 DLY 2230Z-2359Z
08-10 Feb 22 DLY 2230Z-2359Z
Duration: *Emitter events may last the entire requested period, but not guaranteed*

These times represent the potential time slots in which the emitters could be transmitting RFI in the form of CW. A set of 24 Spire's satellites that carry the STRATOS receivers were considered in the scheduling process. Attitude changes were not done, so that usual GNSS-R/RO processes were affected as little as possible during the test. Examples of an unfavorable pass and a favorable pass are shown below in Figures 4-5.

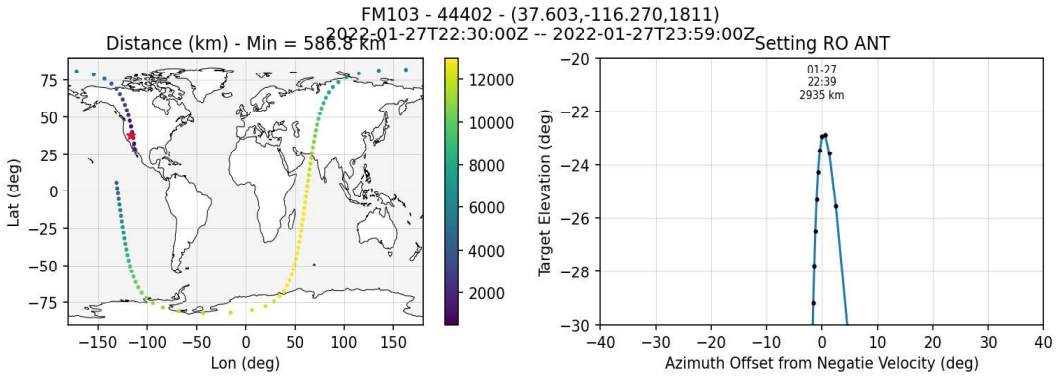

Figure 4 - Unfavorable collection scenario. While the elevation is good (as measured from East-North plane of satellite position to the mean of the provided emitter locations), the North-South, horizon-facing orientation of the GNSS-RO satellites makes this unlikely to be a good candidate for the reception of the emitters CWs with good SNR.

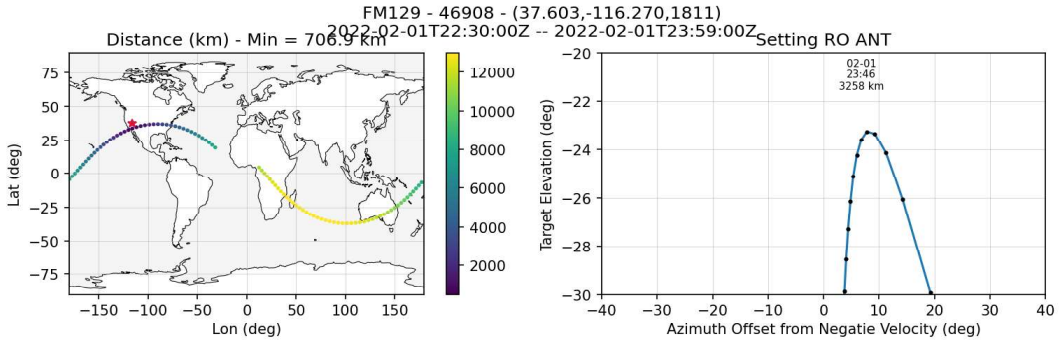

Figure 5 - Favorable collection scenario. Both elevation and orientation of the RO antennas with respect to the satellite attitude are good. The North-facing RO antenna will be directly facing the emitter locations, thus receiving the emitters CWs with best SNR.

Six favorable passes were chosen and recorded, with four of them capturing RFI. All of them were recorded by GNSS-RO satellites. They are summarized in Table 1.

Table 1- Successful collections. Note that Spire's satellites are internally referred to as "FM" (Flight

Module) and a uniquely identifying number.

Collect	FM	Start Time	Duration (sec)	Collection Result
1	FM103	2022-01-27T22-31-40Z	120	Success, but no transmission
2	FM119	2022-02-03T22-36-20Z	120	Success, transmission during first 5 seconds
3	FM119	2022-02-04T22-37-00Z	120	Success
4	FM128	2022-02-04T22-38-30Z	120	Success
5	FM129	2022-02-01T23-40-00Z	120	About 2.7 sec gap in L2 data
6	FM129	2022-02-04T23-37-00Z	120	Success, but no transmission

4 ANALYSIS

4.1 PVT Accuracy

This section compares the real-time OBS and the POD calculated on the ground in post-processing.

Spire had previously compared 45 orbit collections between 2017-04-25 and 2017-05-01, each over an hour duration. The POD is produced using RTOrb, which quotes decimeter accuracies for LEO orbits and is regarded as ground truth in the following. Both the POD and OBS are computed at 1 Hz intervals, but the POD solution is interpolated to the time stamps of the OBS. Generic takeaways showed that orbital and clock errors combined resulted in model delay errors of 12 meters RMS over the 45 orbit collections. It should be noted that the RMS difference for the last 30 minutes of each navigation solution had an RMS range error of about 12 meters, decreasing to about 5 meters for the last 10 minutes. It was found that the PVT engine takes roughly 10 minutes to converge to mainly values below 20 meters, as it is based on a Kalman filter.

As a result, for all collections, the OBS is considered after the initial 10-minute transient time, so that it can achieve maximal accuracy. For all 6 collections processed, the absolute error in ECEF Cartesian coordinates is less than 50 m in position, 0.3 m/s in velocity, and 0.2 µs in clock bias, on average, for each pass. An example from Collection #5 is shown in Figure 6.

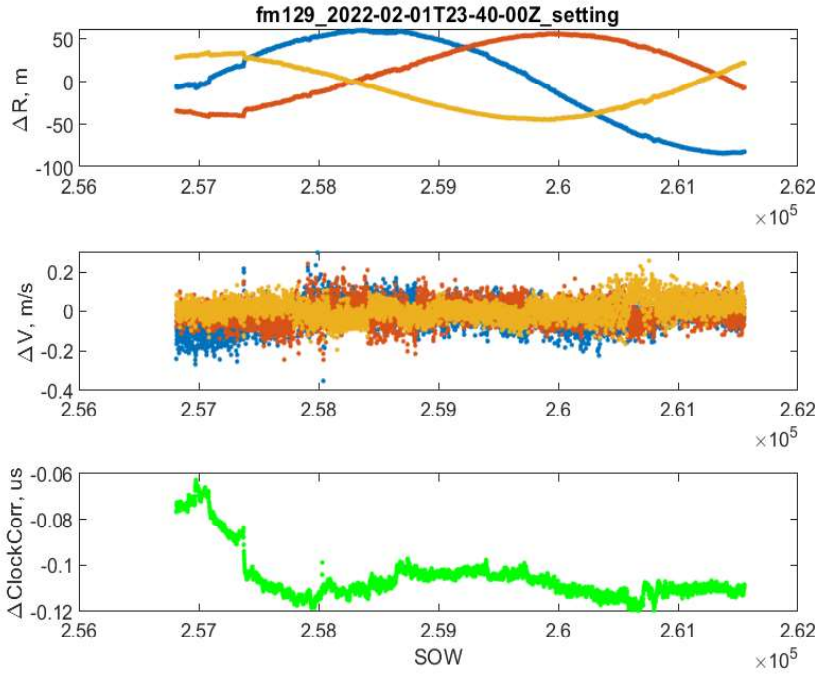

Figure 6 - OBS error for Collection #5.

4.2 Receiver Offset

Since the on-board GNSS receivers are in LEO and stay operational for years, they tend to accumulate various systematic errors. Especially, it is pivotal that the reference oscillator offset error is mitigated to minimize the error due to the receiver clock drift on Doppler estimates, either in single or multiple satellite geolocation methods. Post-processing algorithms exist to jointly estimate both emitter(s) location and receiver frequency offset but suffer from large solution spaces and non-trivial ambiguities. If the receiver offset can be successfully compensated for by using the OBS, this paves the way for more accurate geolocation in post-processing and eventual onboard geolocation.

What is presented here is another post-processing methodology using the OBS to explicitly estimate and mitigate the receiver frequency error. Each data collection is accompanied by a precise GPS timestamp of the record start and OBS which allows one to evaluate the expected Doppler frequency of the signal as well as the receiver's reference clock rate.

$$\Delta f = -f_c \frac{(\boldsymbol{T}-\boldsymbol{R})^T \boldsymbol{V}_R}{|\boldsymbol{T}-\boldsymbol{R}| c_0} \qquad (1)$$

Where f_c is the carrier (i.e., L1 or L2), c_0 is the speed of light, and T and R are the ECEF coordinate vectors of the transmitter and satellite receiver, whose velocity is denoted by V_R. Receiver position and velocity are functions of the GPS time and are estimated as part of the OBS. The static transmitter position is assumed as provided from the public notice.

At the receiver, L1 and L2 signals are down-converted to the IF and digitized. The down-conversion and ADC are driven by the same reference clock. Therefore, the clock drift results in a frequency offset of the sampled IF data. The OBS provides the clock bias correction with respect to the best estimate of GPS time. At first, this correction is approximated by a second order polynomial during the collection time (~120 seconds). The error of such approximation within the relatively short time interval is less than 1 ns. Secondly, the polynomial approximation enables the estimation of the clock drift, which is the dimensionless ratio of the clock bias correction to the clock rate (over 1 s). The clock drift results

in an offset of the digitized signal frequency: a positive clock drift corresponds to a slower receiver clock and, consequently, to a higher apparent signal frequency. The incoming signal frequency is corrected by adding the following offset estimate:

$$f_{offset} = -f_c \frac{\Delta\tau_{clk\_corr}}{\Delta t_{clk}} \quad (2)$$

Where $\Delta\tau_{clk}$and Δt_{clk} are the clock bias correction and clock rate, respectively. As an example, the estimated frequency offset to correct the receiver frequency for Collection #3 is shown in Figure 7.

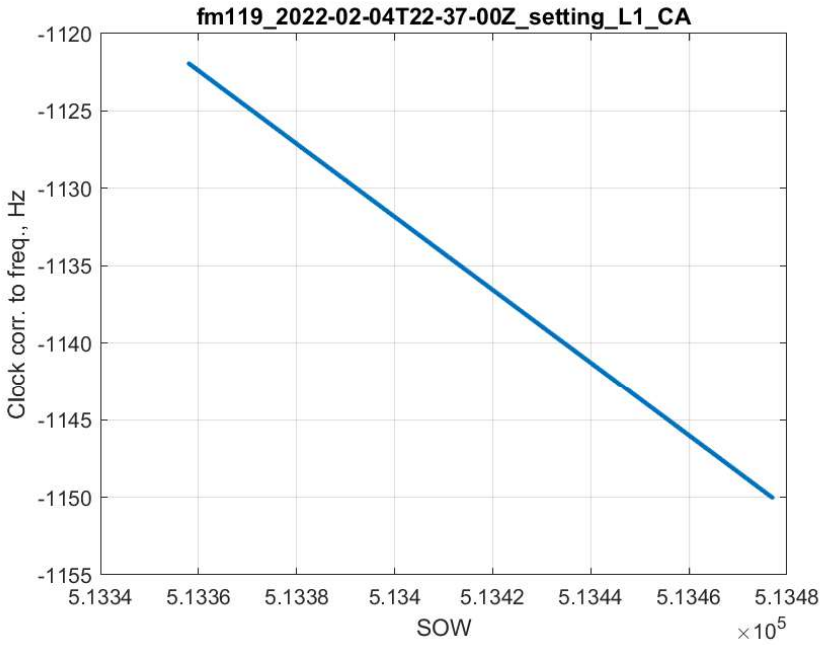

Figure 7 - Example of frequency correction from Collection #3.

After removing the offset with the provided emitter locations in both L1 and L2 bands, the ideally offset-free Doppler curves could be plotted as in Figure 8.

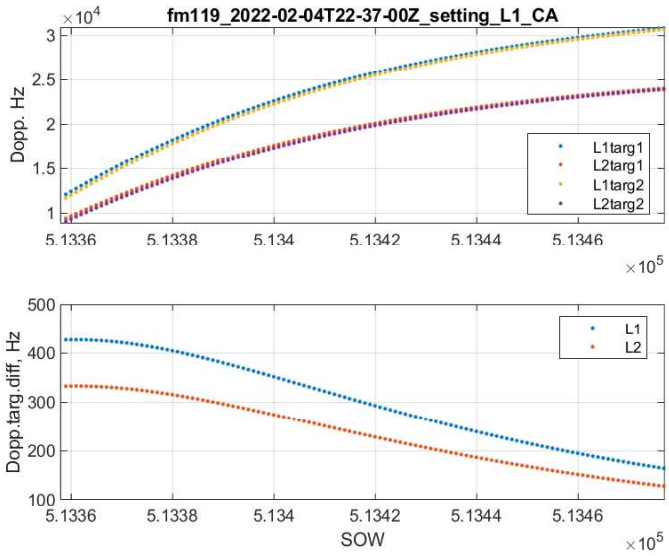

Figure 8 - Ideal Doppler curves for provided emitters.

To compare the observed and expected signals, we identified the 5 strongest maxima of the spectrum at each moment in time. Figure 9 shows the frequencies of such maxima after subtracting the expected Dopplers and clock corrections within a sliding window in time. The top panel corresponds to the subtracted Doppler from the first emitter end the bottom panel from the second emitter. The pink line shows the expected Doppler difference (see Figure 1 bottom panel - the line is overlapped with the maxima points in the top panel). The significant narrow bars correspond to the CW lines at constant frequency in Figure 10.

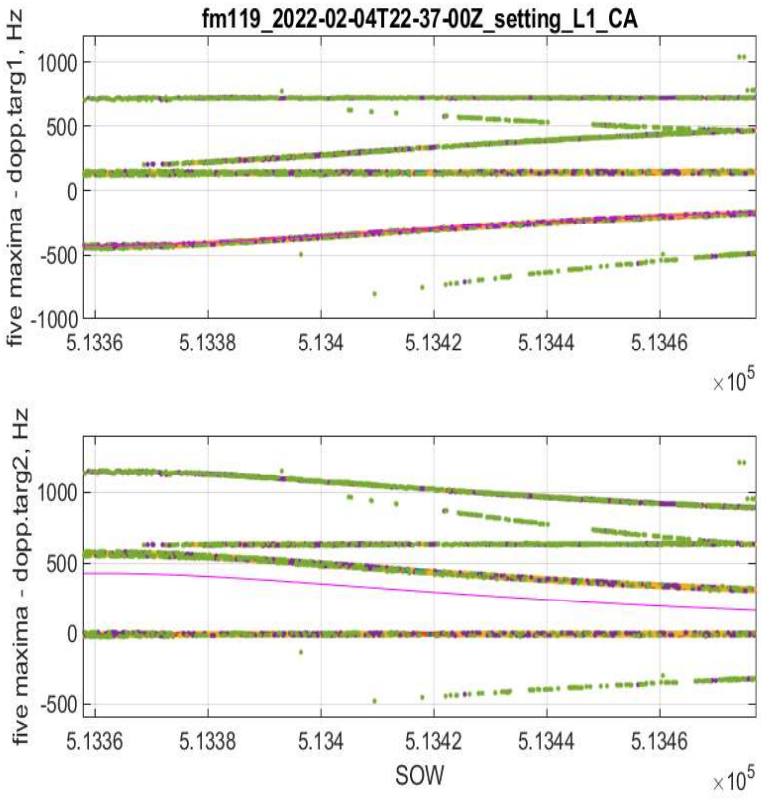

Figure 9 – L1 spectral maxima minus expected Doppler with frequency offset correction.

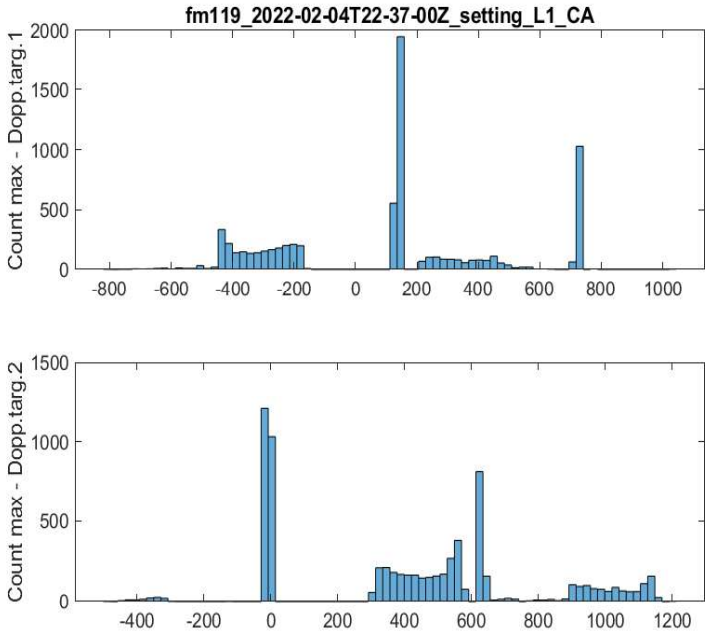

Figure 10 - Histogram of Figure 9.

Clear isolation of the CWs lines helps to plot a more detailed distribution of the deviation of the spectrum maxima frequency from the expected Doppler frequency (Figure 11). The top two panels refer to the first emitter and the bottom one to the second emitter. The width of the distributions is about 15-20 Hz, i.e., the transmit frequency is highly stable. Note, that the spectrogram resolution is about 12 Hz, so narrower variations cannot be distinguished. The frequency separation between two maxima is different for two targets: 582 Hz and 639 Hz (). That allows us to suggest that the two-harmonic structure of the signal is not an artefact of the receiver front end and/or ADC.

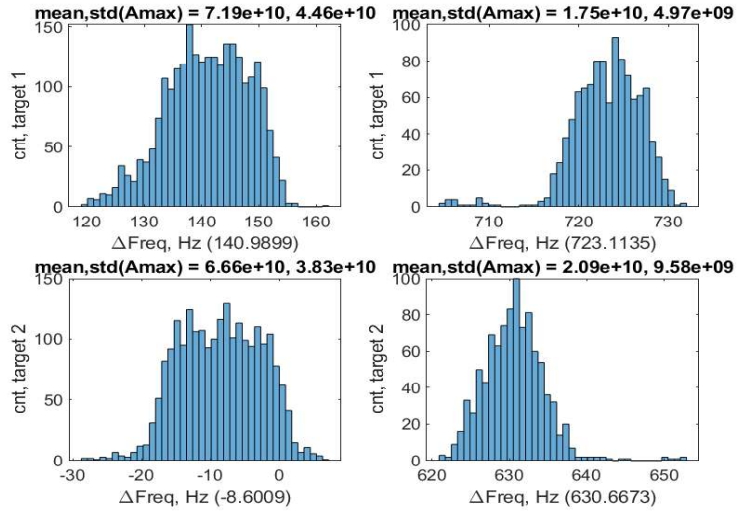

Figure 10 - Detailed distribution of the "stationary" spectrogram maxima. The mean values of the maxima frequency are given in x-labels in parenthesis.

Ultimately, the OBS satisfactorily mitigates receiver errors as it pertains to the geolocation methods Spire intends to use. Further analysis done for Collections #3, #5, and #6 at both L1 and L2 follow the same trends and magnitudes as noted before. General deviations in errors of 200-600 Hz are certainly

acceptable and able to be modelled and contained by statistically based algorithms.

4.3 Single Satellite Geolocation

With ~40 GNSS payloads capable of collecting IF data spread uniformly over the globe, temporal revisit rate and geographic coverage are quite consistent. However, since most of the satellites are spread out in a Sun-Synchronous Orbit (SSO), simultaneous collections from the same areas with multiple satellites happen sporadically. Consequently, geolocation is done with a single satellite and higher collection rates. Spire has spent considerable amounts of time developing proprietary algorithms meant for eventual onboard processing. This algorithm is tested here in a post-processed fashion on Collection #3. It is offered as a proof-of-concept demonstration of the geolocation capabilities of GNSS-R and GNSS-RO satellites with the PVT accuracies and receiver frequency-offset mitigation techniques referenced in the previous section.

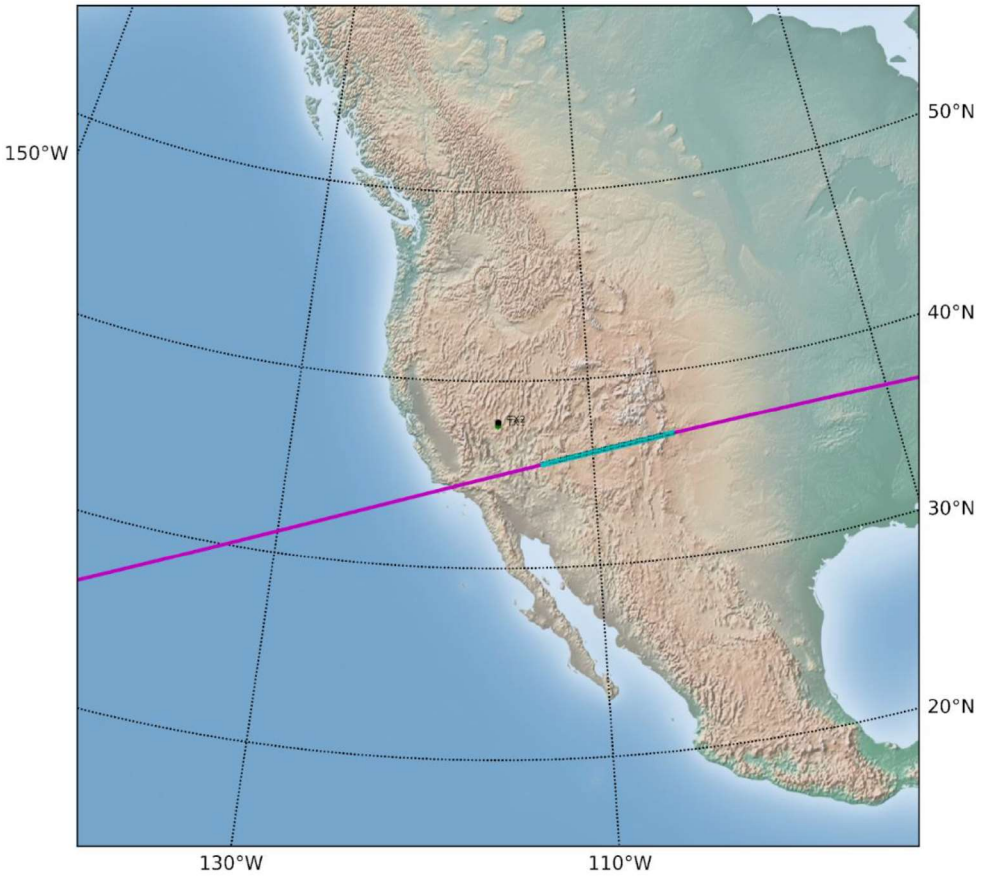

Figure 11 - Satellite track is in magenta while the collection location of the satellite is in green. The two provided emitters are shown in the black and green dots denoted as "TX1" and TX2".

As done before, 5 peaks were identified at each time as the maxima of the spectrogram and the relevant Doppler curves are extracted. Here, only strongest signal in terms of power is geolocated. The results are both with and without correction of the receiver frequency offset.

Fc correction	Lat (deg)	Lon (deg)	Alt (km)	X-std (km)	Y-std (km)	Z-std (km)	Distance from TX1 (km)
No	40.46	-119.84	0	11.7665	8.599.39	4.9221	~420
Yes	37.83	-116.1	0	11.723	8.3241	4.615	~15

The frequency offset mitigation based on the OBS is significantly effective in improving the accuracy of the emitter geolocation.

4.4 Multiple Satellite Geolocation

By leveraging the clock-orbit data of GNSS-R/RO satellites, it is possible to experiment geolocation algorithms with TFDOA measurements from multiple satellites. This is possible in the event of a so-called conjunctions, when two or more satellite fly approximately over the same area. Satellites can be automatically tasked to simultaneously collect IF data in such events.

Conjunction events generally occur a specific area between one and two times a week. Even though this occurrence does not allow for a continuous monitoring of the RF signals in the area of interest, it opens to the proof-of-concept demonstration of Multiple Satellite Geolocation (MSG) algorithms based on the growing fleet of Spire's satellites. In preparation for these collections of multiple and simultaneous datasets, Cramer-Rao Lower Bounds (CRLB) on the geolocation estimate of a variety of signals of interest were calculated for a typical fly-by.

As a case study, the CRLB is evaluated for a conjunction event near a well-documented Syrian GNSS jammer that has been emitting matched-spectrum RFI for several years. The geolocation of this source of was first publicly determined by the Radionavigation Laboratory at the University of Texas at Austin in 2019. According to [1], the emitter has been quoted at being located at 35.4155 N and 35.9420 East right on Russia's Khmeimim Air Base in western Syria and has been plaguing planes flying over Israel.

The hypothetical conjunction event subject of study is shown in Figure 13, in which three satellite fly around the jammer along two different orbits.

Here, the CRLB evaluates the minimum variance of the errors by an unbiased estimator, which indirectly infers the hidden and deterministic source geolocation from TFDOA measurements of the received RFI by the three satellites. Two variants of the CRLB are examined: the usual "unconstrained" estimation, which is purely based on the Fisher information matrix, and the "altitude-constrained" estimation, in which the jammer geolocation is assumed to lie on the Earth's ellipsoid, as proposed in [2]. The statistics of the errors derived from these bounds are reported in terms of Circular Error Probable (CEP) deviation for the constrained CRLB, while both horizontal CEP and Vertical Error Probable (VEP) deviations are reported for the unconstrained CRLB. These deviations are calculated with a 90% probability from Gaussian distributions.

At the coordinates of the emitter, the CEP deviation with altitude constraint is about 13 m on the East-North plane. This horizontal error deviation does not include any bias introduced by an erroneous altitude assumption and it increases to 563 m when no constraint is in place. This increase is expected. In fact, without a fix altitude, the estimation error affecting the vertical component (i.e., along the Up axis) has larger deviation values and is about 1360 m at the jammer location. This is a consequence of the low altitude diversity of satellite orbits.

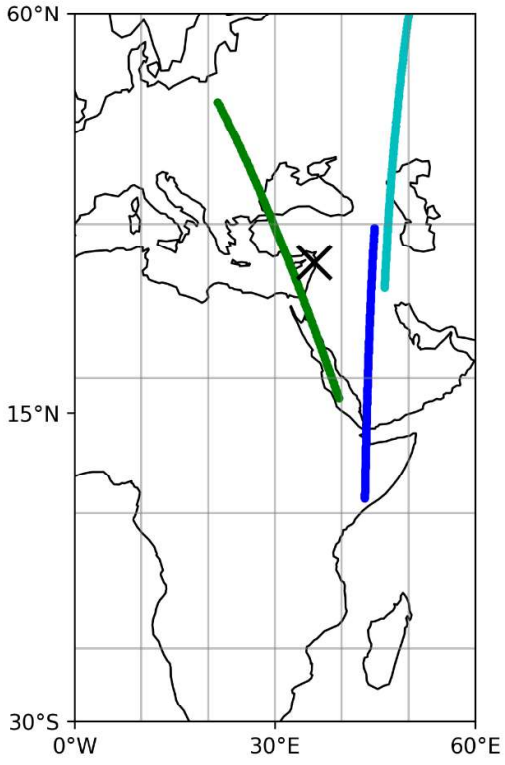

Figure 13 – Conjunction event of the case study. The cross marks the location of the Syrian jammer, the colored lines are the 10-min arcs of the three satellite orbits flying over the jammer at 550 km

The geolocation error deviations derived from the CRLBs are calculated over a ground surface of side 2000 km that is centered at the Syrian GNSS jammer. They are shown in Figure 14, 15, and 16.

of altitude.

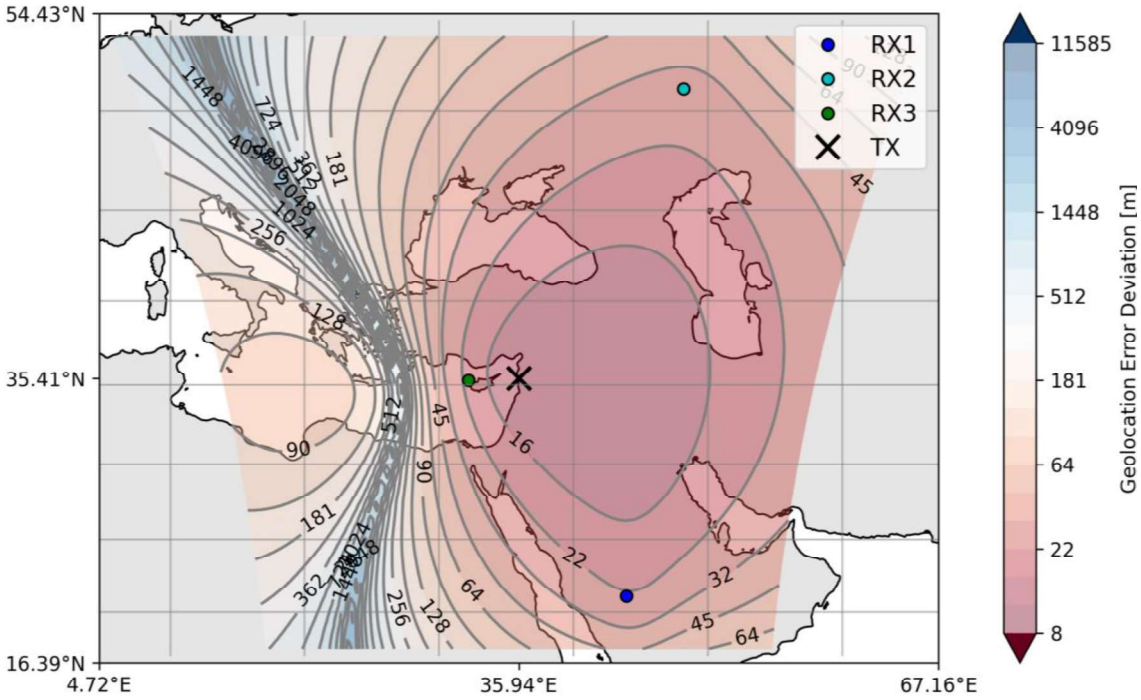

Figure 14 – CEP deviations obtained by calculating the CRLB constrained to zero altitude.

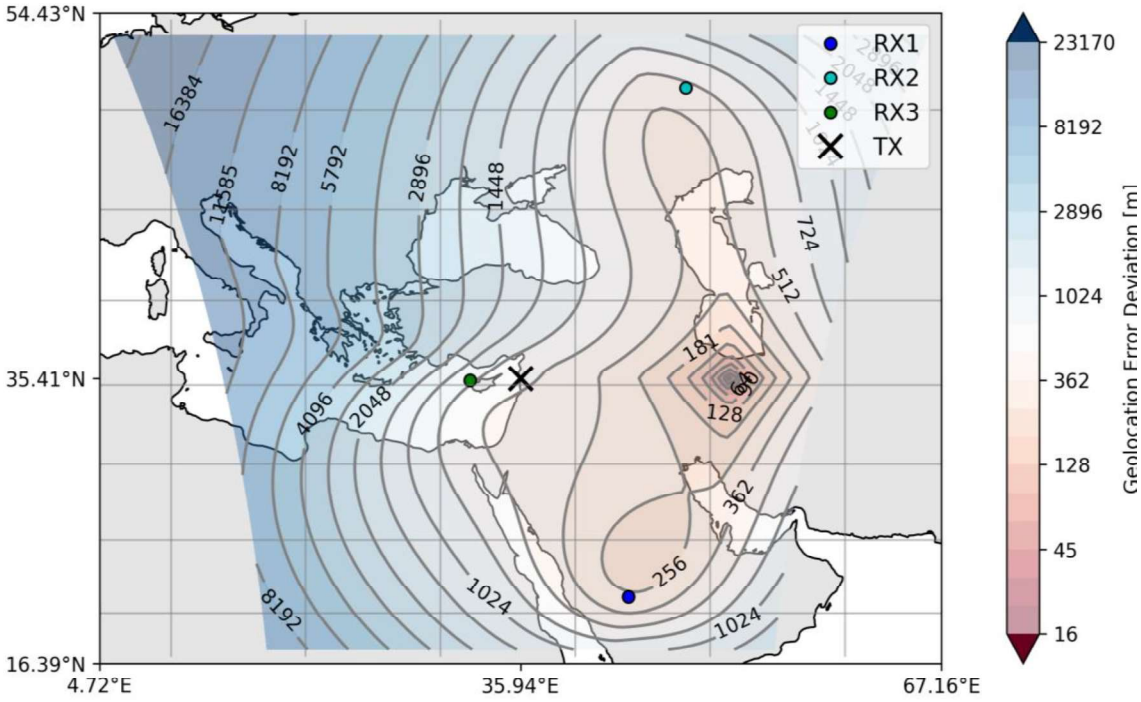

Figure 15 – CEP deviations derived from the unconstrained CRLB.

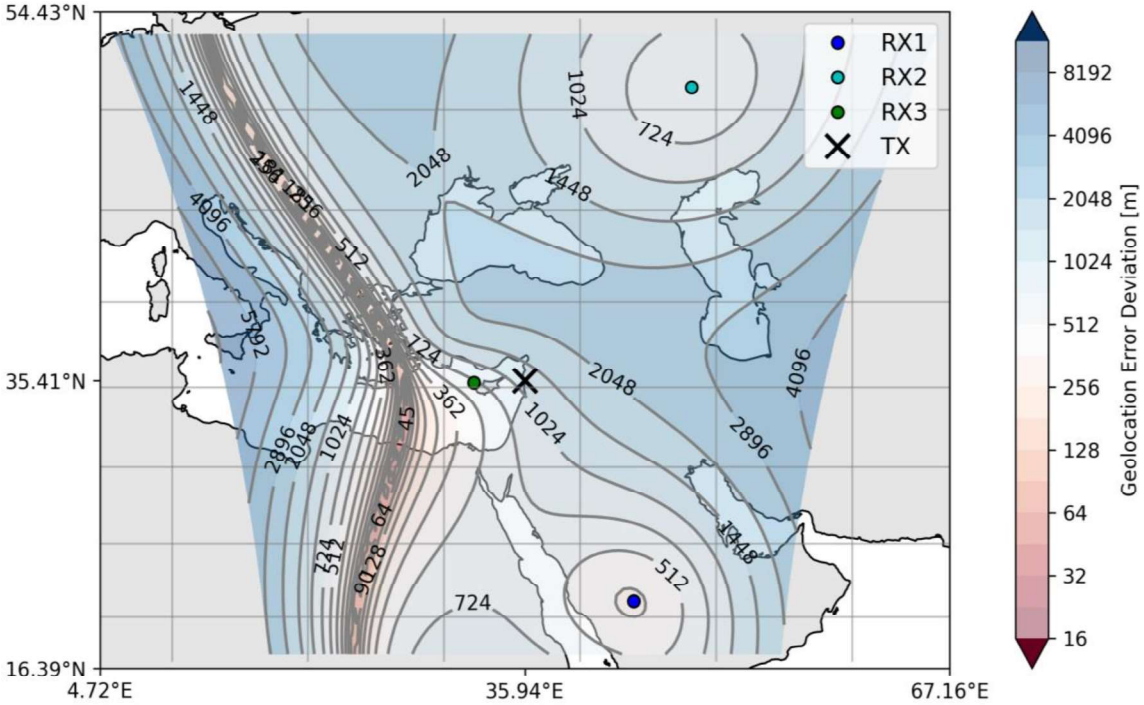

Figure 16 – VEP deviations derived from the unconstrained CRLB.

The CRLBs consider the errors on the TFDOA measurements, which are introduced through the respective and well-known TDOA and FDOA CRLBs found in [3]. For this calculation, the receiver characteristics assumed are listed below, while the received RFI power is evaluated with a dynamic link budget that includes also the actual radiation pattern of Spire GNSS-R satellite antennas. Errors due to residual clock bias and reference oscillator offset are added in the form of additive Gaussian random errors, such as in [4]. Errors on the knowledge of the satellite positions are considered negligible compared to the previous residuals, since it is assumed that the geolocation algorithms will be initially relying on the satellite POD, which is carried out in post-processing.
One last remark concerns the kind if jamming attack under study. As reported in [1], the transmit power of the jammer is about 49 dBm assuming an isotropic antenna in transmission. This jammer is modulating interference with Pseudo-Random Noise (PRN) codes (some of which are used by GNSS satellites) in order to overpower the spectrum of the victim signals, in this case GPS L1 C/A. This information could be exploited to recover some processing gain through correlation (as done for authentic GNSS signals) and, thus, to obtain more accurate TFDOA observables and ultimately more accurate jammer geolocation estimates. Nonetheless, in this paper, only the cross-correlation method is considered for measuring the TDOA and FDOA of received RFI, because the interfering signal structure is generally unknown.

Integration time (ms)	RX noise temperature (K)	RX BW (MHz)	Clock error std (ns)	XO offset std (Hz)
1	375	4	20	10

5 CONCLUSIONS

The ability to utilize GNSS-R/RO satellites for GNSS jamming detection and geolocation is clearly showcased. From a technical requirements standpoint, the ephemeris accuracy, timing accuracy, and integrity of the raw IF collected was proven to provide meaningful geolocation results. Spire is actively applying these capabilities to algorithms based on TFDOA signal measurements and expanding to their entire constellation of 40+ GNSS-R/RO satellites.

6 REFERENCES

[1] Murrian, MJ, Narula, L, Iannucci, PA, et al. *First results from three years of GNSS interference monitoring from low Earth orbit*., Journal of the Institute of Navigation, Volume 68, Number 4

[2] K. C. Ho and Y. T. Chan, *Geolocation of a known altitude object from TDOA and FDOA measurements*, in IEEE Transactions on Aerospace and Electronic Systems, vol. 33, no. 3, pp. 770-783, July 1997

[3] S. Stein, *Algorithms for ambiguity function processing*, in IEEE Transactions on Acoustics, Speech, and Signal Processing, vol. 29, no. 3, pp. 588-599, June 1981

[4] D. CaJacob, et al. *Geolocation of RF Emitters with a Formation-Flying Cluster of Three Microsatellites*, Small Satellite Conference, 2016